The Role of the Maritime Continent SST Anomalies in Maintaining the Pacific–Japan Pattern on Decadal Time Scales

MINGMEI XIE,[a,b] CHUNZAI WANG,[a,c,d] and SHENG CHEN[a,c,d]

[a] *State Key Laboratory of Tropical Oceanography, South China Sea Institute of Oceanology, Chinese Academy of Sciences, Guangzhou, China*
[b] *University of Chinese Academy of Sciences, Beijing, China*
[c] *Southern Marine Science and Engineering Guangdong Laboratory (Guangzhou), Guangzhou, China*
[d] *Innovation Academy of South China Sea Ecology and Environmental Engineering, Chinese Academy of Sciences, Guangzhou, China*

(Manuscript received 19 July 2021, in final form 18 October 2021)

ABSTRACT: The decadal Pacific–Japan (PJ) pattern, the dominant decadal mode of summer vorticity anomaly over East Asia, is characterized as a meridionally arranged wave pattern with one anomalous cyclone located over Taiwan, and two anomalous anticyclones around the South China Sea (SCS) and the Bohai Sea. This pattern can cause wetter and colder conditions in Southeast China and dryer and warmer conditions in North China. The local SST–rainfall relationship reveals that the Maritime Continent (MC) SST can act as an engine to regulate and maintain the decadal PJ pattern. Driven by enhanced convection over the MC, anomalous divergent flows in the upper troposphere move northward, cross the equator, and then converge and subside over the SCS. The SCS low-level divergence, maintained by this meridional overturning circulation under the Sverdrup vorticity balance, further works as a Rossby wave source and excites the decadal PJ pattern pointing straight northward. The transhemispheric impacts of the MC SST are well reproduced by both the atmospheric general circulation model and the dry linear baroclinic model, with the former emphasizing the MC's original forcing role and the latter highlighting the SCS anticyclone's role in relaying and amplifying those climatic impacts. Thus, our results indicate that SST variations over the MC region can be viewed as a potential source of East Asian decadal climate predictability.

KEYWORDS: Maritime Continent; Rossby waves; Teleconnections; Decadal variability

1. Introduction

It has been known that the Pacific–Japan (PJ) pattern or the East Asia–Pacific pattern is the major teleconnection connecting the tropical western North Pacific (WNP) and East Asia (Huang and Li 1987; Nitta 1987) and has significant impacts on the East Asian summer monsoon (EASM) (Huang and Sun 1992; Huang et al. 2012). On intraseasonal to interannual time scales, the PJ pattern, called the *typical PJ pattern* in the present study, is extracted as the leading empirical orthogonal function (EOF) mode of 850-hPa winds or vorticity over summer East Asia (Kosaka et al. 2013; Xie et al. 2016). This leading mode exhibits a tripolar vorticity pattern with alternate signs. Since the high-latitude lobe is relatively weak, the typical PJ pattern is more portrayed as a meridional dipole between tropical (15°–25°N) and midlatitude East Asia (30°–40°N) with an anomalous anticyclonic center over the Philippine Sea and an anomalous cyclonic center over Japan during the positive phase (Kosaka and Nakamura 2006; Wang 2019; Xie et al. 2016; Xu et al. 2019). These atmospheric features of the PJ pattern bring abundant moisture to the Yangtze River valley and the regions to its east, resulting in a prolonged rainfall along the mei-yu–baiu band (Huang 1992; Kosaka et al. 2011). Moreover, the PJ pattern modulates the tropical cyclone genesis and tracks (Du et al. 2011; Kim et al. 2012), and hence affects the livelihood of neighboring inhabitants. Due to the importance of the PJ pattern, considerable efforts have been devoted to understanding the mechanisms responsible for its formation and maintenance from either atmospheric intrinsic, SST-forced, or air–sea coupled views.

First, it is suggested that the typical PJ pattern is an internal dynamical mode that is located in the monsoon–trades confluence zone and obtains energy from the basic flows via barotropic (Lau and Peno 1992) and baroclinic energy conversion (Kosaka and Nakamura 2006, 2010). Through further modeling work, Kosaka et al. (2013) confirmed that the PJ pattern could emerge even if only climatological SST is prescribed, but its variance is only one-third of the total variability. From both the aspects of amplitude and temporal persistence, this atmospheric inherent mode is significantly weaker than the observation and vanishes rapidly, so it is indispensable to consider the external forcing from the oceans on the longer time scales.

The second but earlier view was initially suggested by Nitta (1987) and Huang and Li (1987). They regarded the typical PJ pattern as a Rossby wave train excited by the WNP local SST anomalies, which was later numerically vindicated by Huang and Sun (1992). The SST-related convective activities give rise to the baroclinic structure of the PJ tropical part (Gill 1980; Kurihara and Tsuyuki 1987). Other than local SST forcing, Xie et al. (2009) and Wu et al. (2009) further elaborated that the Indian Ocean warming serves as a remote oceanic

Supplemental information related to this paper is available at the Journals Online website: https://doi.org/10.1175/JCLI-D-21-0555.s1.

Corresponding author: Chunzai Wang, cwang@scsio.ac.cn

DOI: 10.1175/JCLI-D-21-0555.1

source for the typical PJ pattern. The summer Indian Ocean warming causes tropospheric temperature responses, emanating an atmospheric Kelvin wave wedging into the WNP. Accompanying with surface divergence, the Kelvin wave strengthens the anomalous anticyclone, which is the tropical lobe of the PJ pattern, to its north flank. This remote forcing maintains the PJ pattern beyond ENSO peaks.

Other alternative viewpoints that involve the interactions between the typical PJ pattern and adjacent climate systems give more advanced and complicated pictures. For example, by using the dry linear baroclinic model (LBM), Lu and Lin (2009) pointed out that the mei-yu precipitation anomalies resulting from the PJ circulation can in turn reinforce this meridional teleconnection via the latent heat release. Kosaka et al. (2013) and Xie et al. (2016) further advanced the Indian Ocean forcing theory by demonstrating that the PJ's elongated anticyclone also contributes to the Indian Ocean warming through the anomalous easterlies at the southern edge of it. The wind-induced suppressed evaporation positively feeds back on the initial warm SST, and thus the typical PJ pattern forms an air–sea coupled mode among the Indo-Pacific regions. In their studies, SST forcing, as the cause of long persistence of the pattern, is crucial and deserves to be investigated on decadal time scales. However, since the major parts of the decadal PJ mode sit atop the land (see section 3b and Fig. 3a), the coupled processes between them and the oceans are not discussed any further.

Many studies have pointed out the salient decadal changes of the EASM (Chen et al. 2019; Ding et al. 2008; Song and Zhou 2015; Zhang et al. 2017), so the motivation to reveal decadal variabilities of the PJ pattern arises spontaneously. At the mid-to-late 1990s, the typical PJ pattern experienced an eastward shift in active centers, weakened coupling of vertical structures (Xu et al. 2019), and a reduction in periodicity (Chen and Zhou 2014; Sui et al. 2007; Wu and Zhou 2008). These all indicate that there might be a decadal variation residing in the climate of the tropical WNP and East Asia. Based on temporally filtered wind anomalies, Wu et al. (2016) investigates the dominant low-frequency modes of the EASM through multivariate EOF (MV-EOF) analysis. They defined the leading mode as the *decadal PJ pattern*, which is shaped as a cyclonic center over Taiwan and an anticyclonic center over the Bohai Sea [see our Fig. S1 in the online supplemental material and also Fig. 3a of Wu et al. (2016)]. The decadal PJ pattern shares some similar dynamical characteristics with the typical PJ pattern, like the Rossby wave nature and the tilted vertical structure. However, it is worth noting that there are at least three differences between the decadal PJ pattern and the typical one. Compared with the typical PJ pattern, the low-level wave train of the decadal PJ pattern possesses equatorward shifted centers by about 8° of latitude, a zonally confined extent within eastern China, and straight northward propagation (see section 4 for detailed comparisons). Along with the two centers recognized by Wu et al. (2016), this low-level wave train actually shows a meridional tripolar structure emanating from the South China Sea (SCS). Recently, an anomalous anticyclone over the SCS is found to be associated with the decadal variability of the Maritime Continent (MC) SST (Xie and Wang 2020). This suggests that the SCS anomalous anticyclone may act as a bridge to relay the decadal variability of MC SST to East Asia. In this study, we will explore the potential impacts of MC decadal SST variations on the decadal PJ pattern from atmospheric reanalysis, and use a simple dry atmospheric model (i.e., LBM) and an atmospheric general circulation model (i.e., CAM4) to further validate the basic processes.

The paper is organized as follows. Section 2 introduces the datasets and methodology used in this study. Section 3 describes the decadal MC variation and its relationship with the decadal PJ pattern. Section 4 gives the underlying physical mechanisms and numerical modeling results. Conclusions and discussion are presented in section 5.

2. Datasets, methods, and model

a. Datasets and methods

Here, we focus on the period from 1900 to 2012. The long-term precipitation and the atmospheric circulation fields are adopted from the Twentieth Century Reanalysis (20CR) dataset (Compo et al. 2011). Monthly SST data come from the NOAA Extended Reconstructed Sea Surface Temperature version 5 (ERSSTv5) dataset (Huang et al. 2017). The ECMWF Coupled Earth Reanalysis of the twentieth century (CERA-20C; Laloyaux et al. 2018) and HadISST1.1 datasets (Rayner et al. 2003) are also supplementally used to verify the results. Tables 1 and 2 list multiple long-term observational datasets of land surface air temperature (SAT) and precipitation that are compared with the reanalysis during the same period.

To stress features on large scales, the vorticity and streamfunction fields, which are derived from winds via spherical harmonics, are first triangularly truncated at the wavenumber 42 (T42). We then taper off the nth spherical harmonic component by multiplying a coefficient $\exp\left(-\left\{[n(n+1)]/[N(N+1)]\right\}^{r}\right)$ varying with the wavenumber n (from 1 to 42) to get spatially smoothed fields (Sardeshmukh and Hoskins 1984; Wu et al. 2016). The parameters N and r are set to 24 and 8, respectively. Thus, the amplitude of the harmonic component at $n = 24$ will reduce to $\exp(-1)$, while the modes ahead of it remain nearly unchanged.

Since this study focuses on the decadal variability, all variables are subjected to a 7-yr low-pass Butterworth filter to remove their interannual variations (e.g., Wu et al. 2016). If not explicitly noted, the statistical significance of correlation and regression coefficients is assessed using a two-tailed Student's t test with the consideration of effective degrees of freedom. The effective degrees of freedom are estimated by the following approximation (Pyper and Peterman 1998):

$$N_{\mathrm{edf}} = \frac{N}{\left(1 + 2r_{X_1}r_{Y_1} + 2r_{X_2}r_{Y_2}\right)}, \tag{1}$$

where N is the sample size and r_{X_j} and r_{Y_j} are the autocorrelations of two sampled time series X and Y at time lag j.

TABLE 1. Descriptions of land SAT datasets used in the study.

Abbreviation/name	Description	Horizontal resolution	Reference
CRU	Global gridded monthly anomalies of observed land air temperature version 4 from the Met Office Hadley Centre and the Climatic Research Unit (CRU) at the University of East Anglia	5° × 5°	Jones et al. (2012)
GHCN	Gridded mean temperature anomalies from the Global Historical Climatology Network–Monthly (GHCN-M) version 4 temperature dataset	5° × 5°	Jones and Moberg (2003), Menne et al. (2018)
UDel	Global gridded monthly high-resolution terrestrial air temperature (version 5.01) compiled from multiple sources and produced by the University of Delaware	0.5° × 0.5°	Willmott and Matsuura (2001)
C-LSAT	China land surface air temperature version 2.0	5° × 5°	Sun et al. (2021)

A widely used diagnostic tool named the wave activity flux is calculated following Takaya and Nakamura (2001). Under pressure coordinates, its zonal and meridional components are

$$\mathbf{W} = \frac{1}{2|\mathbf{U}|}\begin{Bmatrix} \overline{u}\left(\psi_x'^2 - \psi'\psi'_{xx}\right) + \overline{v}\left(\psi'_x\psi'_y - \psi'\psi'_{xy}\right) \\ \overline{u}\left(\psi'_x\psi'_y - \psi'\psi'_{xy}\right) + \overline{v}\left(\psi_y'^2 - \psi'\psi'_{yy}\right) \end{Bmatrix}, \quad (2)$$

where $\mathbf{U} = (u, v)$ and ψ denote the horizontal wind velocities and streamfunction, respectively. Overbars indicate climatological means for the period of 1900–2012 and primes indicate anomalies departing from the mean states. The wave activity flux is parallel to the local group velocity of the quasi-stationary Rossby wave in basic flows, and thus applicable to describe the propagation of atmospheric wave trains (Takaya and Nakamura 2001).

b. Models

We use two types of numerical models to validate the observed results. One is the dry LBM, which has been extensively used to study the atmospheric responses induced by idealized forcing. It is a spectral, primitive equation model linearized about the basic state with all nonlinear interactions between perturbations neglected (Watanabe and Kimoto 2000; Watanabe and Jin 2002). We adopted the dry version with T42 horizontal resolution and 20 vertical sigma levels. The background state was set to JJA (June–August) mean climatology derived from NCEP–NCAR reanalysis. The model applies linear Rayleigh friction and Newtonian damping that mimic dynamical and thermodynamic dissipations. In our study, the damping time scale was set to 1 day for the lowest three levels and the topmost two levels, 15 days for the fourth level, and 30 days elsewhere. Biharmonic horizontal diffusion with a time scale of 1 day was also employed to represent the cascade toward smaller scales. It has been verified that the magnitude of diffusion does not strongly affect the direct response to tropical heating (Ting and Yu 1998) and thus is less important than the damping rate (Geng et al. 2000). In the dry version, the model is forced by a prescribed heating anomaly, which is proportional to the observed precipitation anomaly; that is, a rainfall rate of 10 mm day^{-1} corresponds to a column-averaged diabatic heating rate of 2.5 K day^{-1} (Jin and Hoskins 1995).

The other model containing moist processes is the Community Atmosphere Model version 4 (CAM4; Gent et al. 2011), also functioning as the atmospheric component of the Community Earth System Model (CESM). In the present study,

TABLE 2. Descriptions of land precipitation datasets used in the study.

Abbreviation/name	Description	Horizontal resolution	Reference
GPCC	Monthly land surface precipitation dataset (version 2018) of the Global Precipitation Climatology Centre (GPCC)	2.5° × 2.5°	Schneider et al. (2017)
GHCN	Gridded land precipitation anomalies from the GHCN version 2 monthly precipitation dataset.	5° × 5°	Jones and Moberg (2003)
UDel	Global gridded monthly high-resolution terrestrial rain gauge–measured precipitation (version 5.01) compiled from multiple sources and produced by the University of Delaware	0.5° × 0.5°	Willmott and Matsuura (2001)
CRU	High-resolution gridded precipitation data (version 4.04) of Climatic Research Unit (CRU) time series (TS)	0.5° × 0.5°	Harris et al. (2020), Willmott and Matsuura (2001)

the horizontal resolution of CAM4 is 0.9° × 1.25°, and the vertical coordinate is set to 26 hybrid sigma–pressure levels. CAM4 is aimed at revealing the atmospheric circulation response to a specific SST forcing (Chen and Zhou 2014; Hu et al. 2011), and we perform the control and sensitive experiments (MC run) to isolate the impact ascribed to the MC SST variability. The control run is forced by climatological SST annual cycle. In the sensitive run, composited MC SST anomalies selected by the MC SST index > 1 standard deviation (STD) are added onto the climatological SST from May to September. For both experiments, the model is integrated continuously for 30 years, and the ensemble mean of the last 25 years is used in this study. The MC SST's impact is estimated by the mean differences between the MC run and the control run.

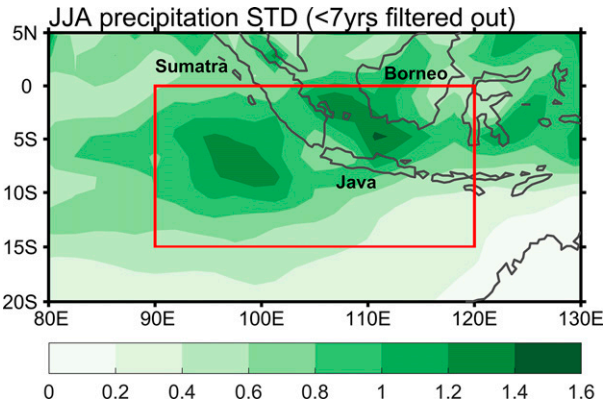

FIG. 1. The STD (mm day^{-1}) of 7-yr low-pass-filtered summer precipitation from 1900 to 2012. The red box in the figure denotes the region 0°–15°S, 90°–120°E, which is used to construct the MC SST index in Fig. 2.

3. The MC decadal variability and its impacts on East Asian climate

a. *Detecting decadal variabilities in the MC region*

Surrounded by the warmest climatological SSTs, higher than 28°C, the MC region is a primary source of tropical latent heat. Before constructing the MC SST index, we want to figure out if the MC region has strong convective variations on decadal time scales. The latent heat released by deep convection is represented by precipitation. Figure 1 shows the STD of summer (JJA) mean precipitation anomaly for the period of 1900–2012. Recall that all variables hereafter are calculated based on the low-pass-filtered fields with interannual variations removed. The large values of the STD with an average at about 0.8 mm day^{-1} overlie the coastal water off Sumatra and extend eastward to Java and Borneo, implying significant latent heat release or reduction on decadal time scales occurring over the central to western parts of the MC region.

In the tropics, the local SST–rainfall relationship might be positive, negative, or even insignificant (Lu and Lu 2014; Wang et al. 2005; Wu et al. 2009). Thus, the precipitation variations could be forced locally or remotely. For showing the source of the decadal MC rainfall, point-to-point correlation between precipitation and SST anomalies is conducted (Fig. 2a). Associated with remarkable enhanced convective activities, significantly positive SST anomalies are located in the marginal seas of the MC (0°–15°S, 90°–120°E; defined as the domain of the MC SST index). This implies that the SST anomalies in the MC can serve as a potential engine to the atmosphere and account for the large rainfall STD there. Owing to the warm climatology, multiscale convective activities over the MC region have notable effects on both the local and global climate from intraseasonal to interannual time span (Chung et al. 2011; Sui et al. 2007; Wu and Zhou 2008; Yang et al. 2019). Oh et al. (2013) suggested that the reinforced diurnal cycle of convection located over the MC hinders the development of the Madden–Julian oscillation by consuming most of the moist static energy. Xu and Guan (2017) indicated that the SST or rainfall variability in the MC region exerts impacts on the EASM as an independent factor from ENSO. However, little research has been devoted to the decadal variations recognized above, and thus their climate impacts should be noted.

In contrast to the remarkable positive SST–rainfall correlation over the MC region, the local correlation over the SCS and Philippine Sea is weak and even negative. This opposite relationship suggests that the ocean is a passive response to the local atmospheric forcing (Lu and Lu 2014; Wang et al. 2005; Wu et al. 2009) and thus lacks a coupled feedback on the atmosphere above the SCS and Philippine Sea. To grasp the overall variabilities of MC convective activities, we define the areal JJA SST anomaly within the large STD region [denoted by the red (green) box in Fig. 1 (Fig. 2a)] as the MC SST index in this study. The long-term MC SST index does exhibit notably decadal variations with one phase persisting for 5–10 years (Fig. 2b) and the dominant period falling in the range of 8–14 years (Fig. S2).

b. *The decadal PJ pattern and climate anomalies associated with MC SST variations*

To dig out the potential effects of the MC SST variations, we calculate the difference of variables based on positive minus negative phases of the MC SST index. Figure 3a shows the composited difference map of SST and 850-hPa wind anomalies. As expected, prominent SST warming is observed over the MC region. Moreover, a Rossby wave train meridionally propagates from the tropical WNP to East Asia, consisting of two anomalous anticyclones centered over the SCS and the Bohai Sea and one anomalous cyclone centered over southeastern China. This northward wavelike pattern is similar to the PJ pattern defined on decadal time scales (Fig. S1; see also Wu et al. 2016). We conduct MV-EOF analysis to the summer 850-hPa winds over East Asia as Wu et al. (2016) did. The spatial correlation between the 20CR EOF1 (Fig. S1) and composited 850-hPa winds is high, with the spatial correlation coefficients (0°–45°N, 100°–130°E) reaching 0.71 and 0.47 for the zonal and meridional components, respectively. This implies that the MC SST variations largely account for the leading mode of summer East Asian atmospheric

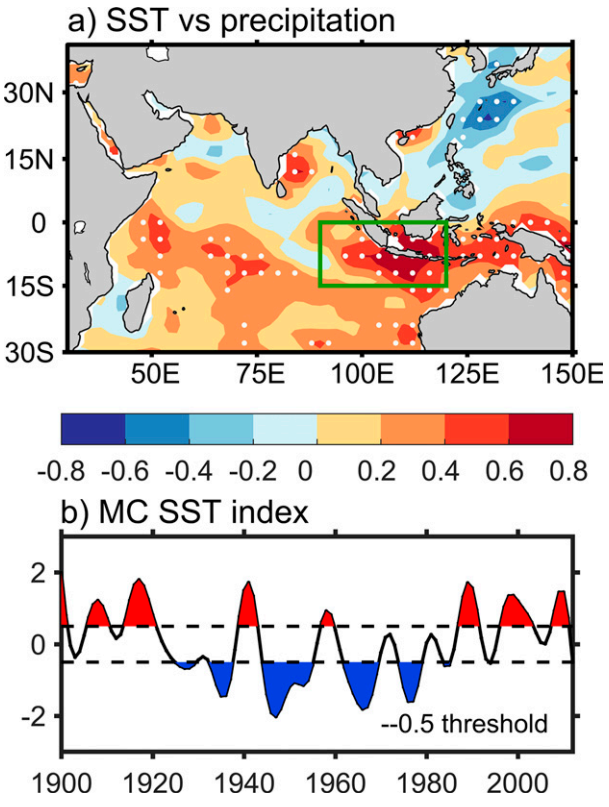

FIG. 2. (a) Point-to-point correlation between SST and precipitation anomalies. White dots indicate the values significant at the 95% confidence level. (b) Standardized time series of the MC SST index. The positive (negative) phase is selected when the MC SST index is greater (less) than 0.5 (−0.5) STD.

circulation on decadal time scales. The reliability of the 20CR results is confirmed by the other long-term dataset (CERA-20C), which is the new-generation ECMWF coupled climate reanalysis adopting a different assimilation strategy from 20CR (Fig. 3b). Above results have verified a close relationship between the MC SST and the decadal PJ teleconnection from the aspect of atmospheric circulation pattern. In contrast to the noticeable warming over the MC, the SST anomalies underlying the decadal PJ pattern are relatively weak, revealing a direct and nonnegligible forcing effect of the remote MC.

The authenticity of Figs. 3a and 3b is further verified by comparing precipitation and SAT anomaly patterns from multiple observational datasets, which show the climatic impacts of the decadal PJ pattern. The composited SAT anomalies from 20CR exhibit a warm–cold–warm tripolar distribution overlapped by the concomitant anomalous circulation. The above-normal SAT in the tropics extends from northern Australia and the MC region to the Indo-China Peninsula and the SCS, which adjoins the below-normal SAT of Southeast China to the north. The other above-normal SAT center is located in North China and connects northwestward with the warming over Mongolia and Siberia, which seems beyond the spatial extent of the decadal PJ pattern (Figs. 3c,d; see also Fig. S3). The cold SST anomalies along the northern SCS coast and the warm SST anomalies within the Bohai Sea are both of the same sign with adjacent SAT anomalies (Fig. 3a) and thus back up the results above. Anomalous meridional temperature advection, vertical motion, and solar radiation contribute to the formation of terrestrial SAT anomalies (Hu et al. 2011; Kosaka et al. 2013). In addition to these, sensible heat transfer from the underlying surface (i.e., SST) plays a dominant role in determining marine SAT anomalies. Therefore, the air over the MC and the SCS is directly warmed by seas. Southerly anomalies on the western part of the two anticyclones carry warm air from lower latitudes to raise the SAT in the southern SCS, the Indo-China Peninsula, and North China. Moreover, the related downward motion gives rise to air warming by adiabatic heating during compression. Analogously, the cyclone-induced upward movement and northeasterly anomalies over southeastern China lower the SAT there with suppressed adiabatic heating and cold advection from northern China.

Precipitation also contributes to the formation of SAT via regulating insolation. Thus, the composited tripolar pattern of precipitation anomaly from 20CR is dynamically consistent with the anomalous winds and SAT, including significant negative anomalies over the southern SCS and Philippines in the tropics and the Bohai Sea in the midlatitudes as well as positive anomalies over Southeast China in the subtropics (Fig. 3e). Increased precipitation corresponds well with moisture convergence and ascending motion of the low-level cyclonic anomalies. A similar relation can also be found between deficient precipitation and anticyclones. Meanwhile, the composite from GPCC also exhibits a meridional tripole, the tropical part of which could be inferred from the decreased rainfall over northern Borneo and southern Philippines (Fig. 3f). The seesaw pattern of mainland China is also evident but with the positive core shifting northward from South China to the Yangtze River valley (comparing Fig. 3f and Fig. S4 with Fig. 3e). Nevertheless, the active western MC convection in all datasets supports this place as a source region for atmospheric heating. The coherent relationship between the 850-hPa wind, precipitation, and SAT anomalies verifies the existence of the decadal PJ pattern, and further reflects its noticeable impacts on the climate of East Asia.

4. Physical mechanisms responsible for the decadal PJ pattern

a. Structure of the decadal PJ pattern

Given the composited prominent wavelike structure and resultant variations of surface variables, in this section we intend to elaborate the horizontal and vertical structures of the decadal PJ pattern associated with MC SST variabilities. Vorticity anomalies (ζ) at the 850- and 200-hPa levels are regressed upon the MC SST index (Fig. 4). In the lower level, there are three meridionally arranged centers with alternating signs extending from the SCS to northeastern China. The cyclonic anomalies around Taiwan are flanked by the SCS and the Bohai Sea anticyclonic anomalies to the south and

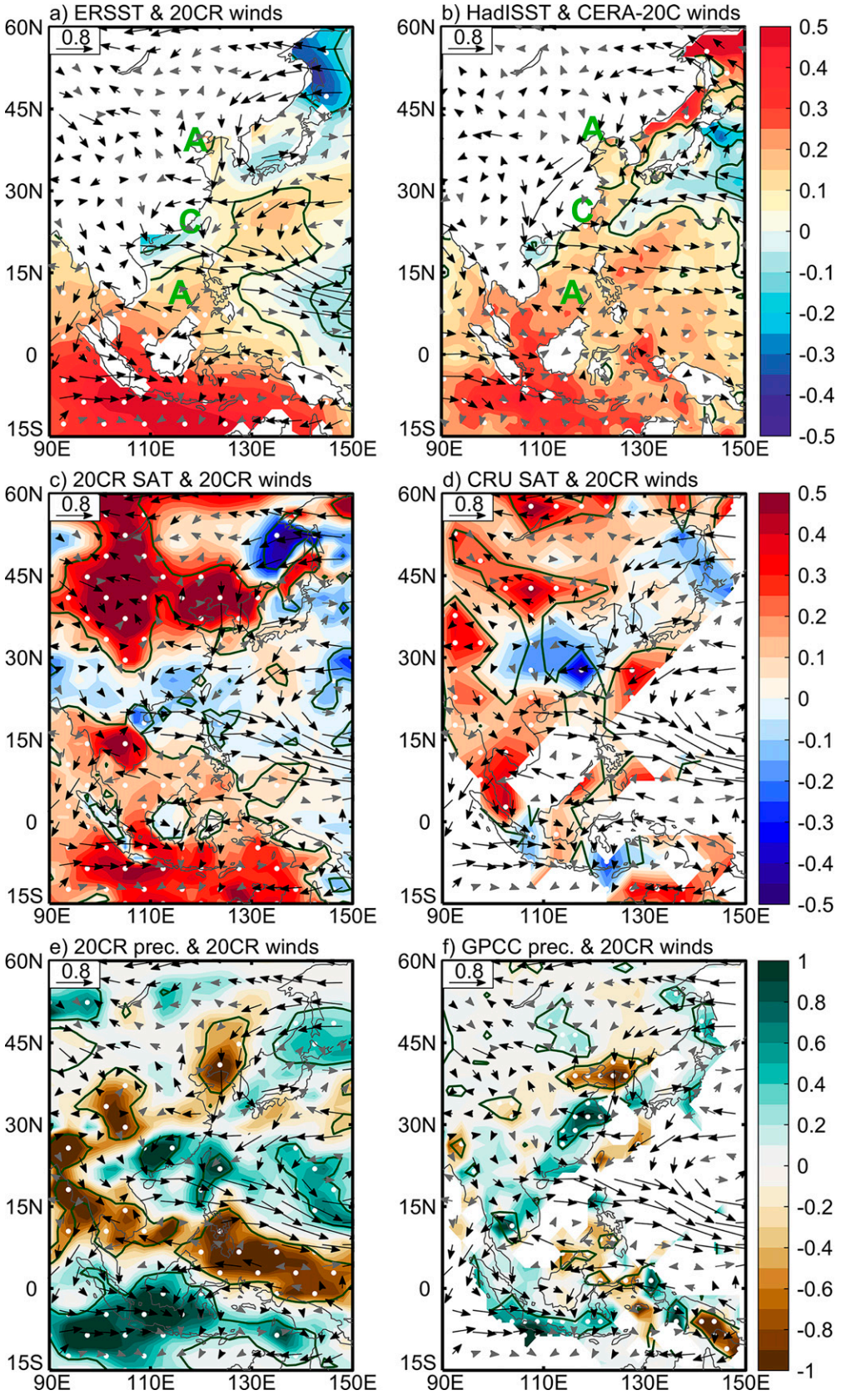

FIG. 3. (a),(b) Composites of JJA SST (shading; °C) and 850-hPa wind anomalies (vectors; m s^{-1}). Black vectors indicate the winds significant at the 90% confidence level based on a one-tailed *t* test. The regions stippled by white dots and encompassed by green lines denote where the values are significant at the 90% confidence

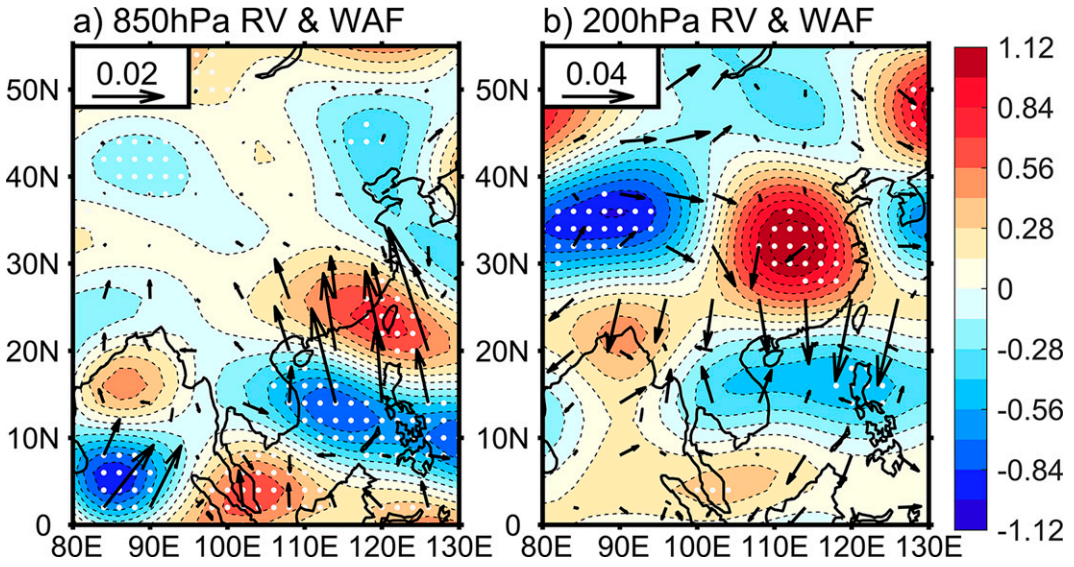

FIG. 4. (a) 850- and (b) 200-hPa regression maps of summer relative vorticity (RV; shading; 10^{-6} s^{-1}) and corresponding wave activity flux (WAF; vectors; m^2 s^{-2}) anomalies onto the standardized MC SST index. White dots denote vorticity anomalies significant at the 90% confidence level.

north, respectively (Fig. 4a). The upper-level vorticity anomalies shift 6°–8° latitude poleward relative to the low-level anomalies, by about one-quarter wavelength (Fig. 4b). From the view of the meridional section along 120°E, the wavelike pattern spreads throughout the entire troposphere and tilts northward evidently (Fig. 5). The cores in the upper level vertically align with the node lines of low-level anomalies (green lines in Fig. 5), which also manifests the downstream shift of one-quarter wavelength. This tilted configuration is basically consistent with the typical PJ pattern's vertical structure raised by Kosaka and Nakamura (2006). They refreshed the traditional view by demonstrating that the typical PJ pattern is a superposition of baroclinic and barotropic modes rather than a distinguishable baroclinic structure in the tropics and an equivalent barotropic structure in the midlatitudes. Here, due to the similarity, the decadal PJ pattern is also identified as a combination of baroclinic and barotropic modes. The barotropic and baroclinic components are separated as $\overline{\zeta} = (\zeta_{250\text{hPa}} + \zeta_{850\text{hPa}})/2$ and $\hat{\zeta} = (\zeta_{250\text{hPa}} - \zeta_{850\text{hPa}})/2$, respectively, following the similar equations of Lee et al. (2009) and Lyu et al. (2017). For the tropical part of the decadal PJ pattern, the ratio of barotropic and baroclinic constituents is close to 1:1.3 (Fig. S5a). Furthermore, the barotropic constituent becomes dominant when it comes to higher latitudes. Lee et al. (2009) and Wang et al. (2010) suggested that the vertical wind shear of basic flows can convert tropical baroclinic signals into extratropical barotropic signals. The latter transmits poleward under the tropospheric mean westerly wind.

The typical PJ pattern was regarded as a Rossby wave train arcing eastward from the tropical WNP (Huang and Li 1987; Nitta 1987; Tsuyuki and Kurihara 1989). To investigate the propagation behavior of the decadal PJ pattern, wave activity fluxes are regressed onto the MC SST index for the both 850- and 200-hPa layers. As embedded in the distinct southerly monsoon flow, the low-level fluxes originate from the middle SCS rather than the MC in the Southern Hemisphere, and propagate straight northward in the lower troposphere (Wu et al. 2016), whereas in the upper layer the fluxes turn to propagate southward over East Asia and seemingly veer from the negative vorticity anomaly over the Tibetan Plateau. The enhanced upper-level propagation suggests that there might be other extratropical factors regulating this decadal pattern, and we will briefly discuss this issue later in section 5.

The decadal PJ pattern bears some resemblance to the typical one because of the same Rossby wave nature. However, salient differences also exist between the two PJ patterns as shown in Fig. 6. First, the low-level cores of the decadal PJ pattern are located more southward. For example, if we regard the first anomalous center that emanates wave activity fluxes as the reference, the decadal PJ pattern starts from the center at ~12°N (Figs. 3 and 4), while the typical PJ pattern starts from ~20°N [cf. Fig. 4 in Kosaka and Nakamura (2006)

←

level based on a two-tailed t test. The composites show the differences for positive minus negative phases of the MC SST index in Fig. 2b. (c),(d) As in (a) and (b), but for the SAT (shading; °C) and 850-hPa wind anomalies (vectors; m s^{-1}). (e),(f) As in (a) and (b), but for the precipitation (shading; mm day^{-1}) and 850-hPa wind anomalies (vectors; m s^{-1}). Datasets used are noted in the title of each subfigure.

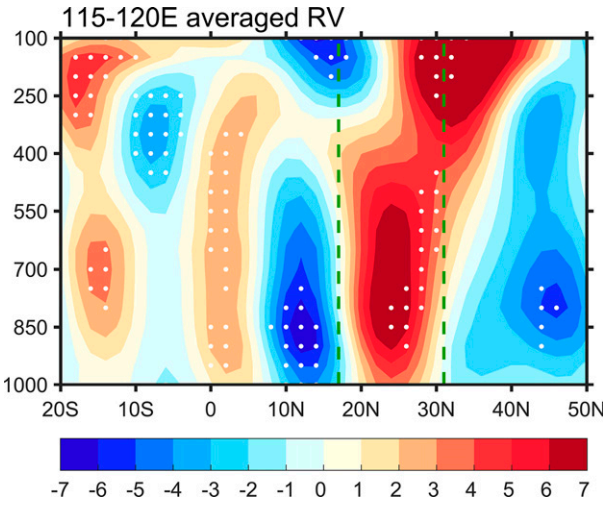

FIG. 5. The latitude–height section (averaged over 115°–120°E) of summer relative vorticity (10^{-7} s^{-1}) anomalies regressed upon the standardized MC SST index. White dots denote vorticity anomalies significant at the 90% confidence level.

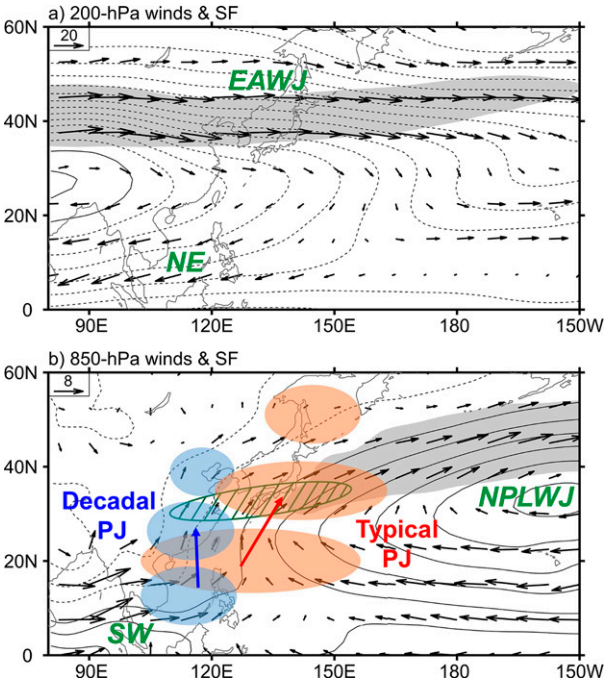

FIG. 6. Climatological JJA winds (vectors; m s^{-1}) and streamfunction (SF; contours; 10^6 m^2 s^{-1}) at the (a) 200- and (b) 850-hPa levels. In (a) and (b), the midlatitude regions where the zonal component of winds is greater than 20 and 4 m s^{-1} are shaded by light gray, respectively. The orange and blue patches denote the schematic distribution of the typical PJ and the decadal PJ, respectively. The green hatched area denotes the mei-yu–baiu band, which is partially overlapped by the westerly jet. SW and NE indicate the monsoonal southwesterly and northeasterly winds.

and others]. Hence, the former shifts equatorward by about 8° latitude compared to the latter. Second, the decadal PJ pattern is primarily confined within the band containing the SCS and eastern China (i.e., between 110° and 130°E), so that the main part of it resides over the land and is weakly coupled with the underlying SST, which limits its zonal range. However, unlike the decadal one, the typical PJ pattern involves various air–sea coupled processes with the tropical WNP to its east (Wang 2000) and the Indian Ocean to its west [Kosaka et al. 2013; cf. Fig. 3 in Xie et al. (2016) for a schematic view] and thus forms a coupled mode spanning the whole Indo–western Pacific Ocean. Last, as clearly denoted by wave activity fluxes, the decadal PJ pattern is meridionally oriented whereas the typical one is southwest–northeast-oriented. The location of each active center seems to be well anchored by the precipitation anomaly. Lu and Lin (2009) have pointed out that the mei-yu–baiu rainband has an indispensable role in shaping the typical PJ pattern. Strong latent heat release from the mei-yu–baiu rainfall induces the eastward shift of anomalous centers and meanwhile intensifies both of the East Asian westerly jet (EAWJ) and the North Pacific low-level westerly jet (NPLWJ), whose waveguide effect is conducive to a deflected wave ray (Fig. 6, orange patches). Nevertheless, the decadal PJ pattern lacks an elongated and continuous rainband as the typical PJ generally has. The absence of significant rainfall anomalies near Japan (Fig. 3e) insulates the decadal PJ pattern from the EAWJ and the NPLWJ, which thus partially accounts for the meridionally straight propagation of it (Fig. 6, blue patches).

Xu et al. (2019) suggested that the PJ pattern's structural change in the late 1990s could be attributed to the movement of the Rossby wave source (convection) over the tropical WNP. For similar reasons, the formation of the decadal PJ pattern is directly relevant to the tropical suppressed convective anomaly near the SCS and Philippines that emanates wave activity fluxes poleward. Furthermore, above three differences between the decadal and typical PJ patterns are likely to be explained by the location and zonal extent of this SCS suppressed convection anomaly. Thus, in the later subsection, we will figure out underlying mechanisms of the SCS suppressed convection that is forced by the decadal MC SST anomalies.

b. Origin and effects of the suppressed convection over the SCS

Foregoing composites have given us a hint about the MC SST's role. To further reveal its dynamical impacts, large-scale divergent winds in both the upper and lower troposphere are regressed onto the MC SST index (Figs. 7a,b). As expected, a decadal warming over the MC is accompanied by anomalous lower-level convergence and upper-level divergence. The outflows from the MC region converge over the SCS, leading to local downward motion and anomalous divergence in the lower level. Vertical change of vertical velocity is well connected with horizontal divergence via the continuity equation: $\partial\omega/\partial p = -\nabla \cdot \mathbf{u}$. At the core of the SCS subsidence (rainfall suppression), horizontal divergence and convergence are strongest at the 950- and 250-hPa levels, respectively (Fig. S5b), while the low-level negative vorticity extremum is

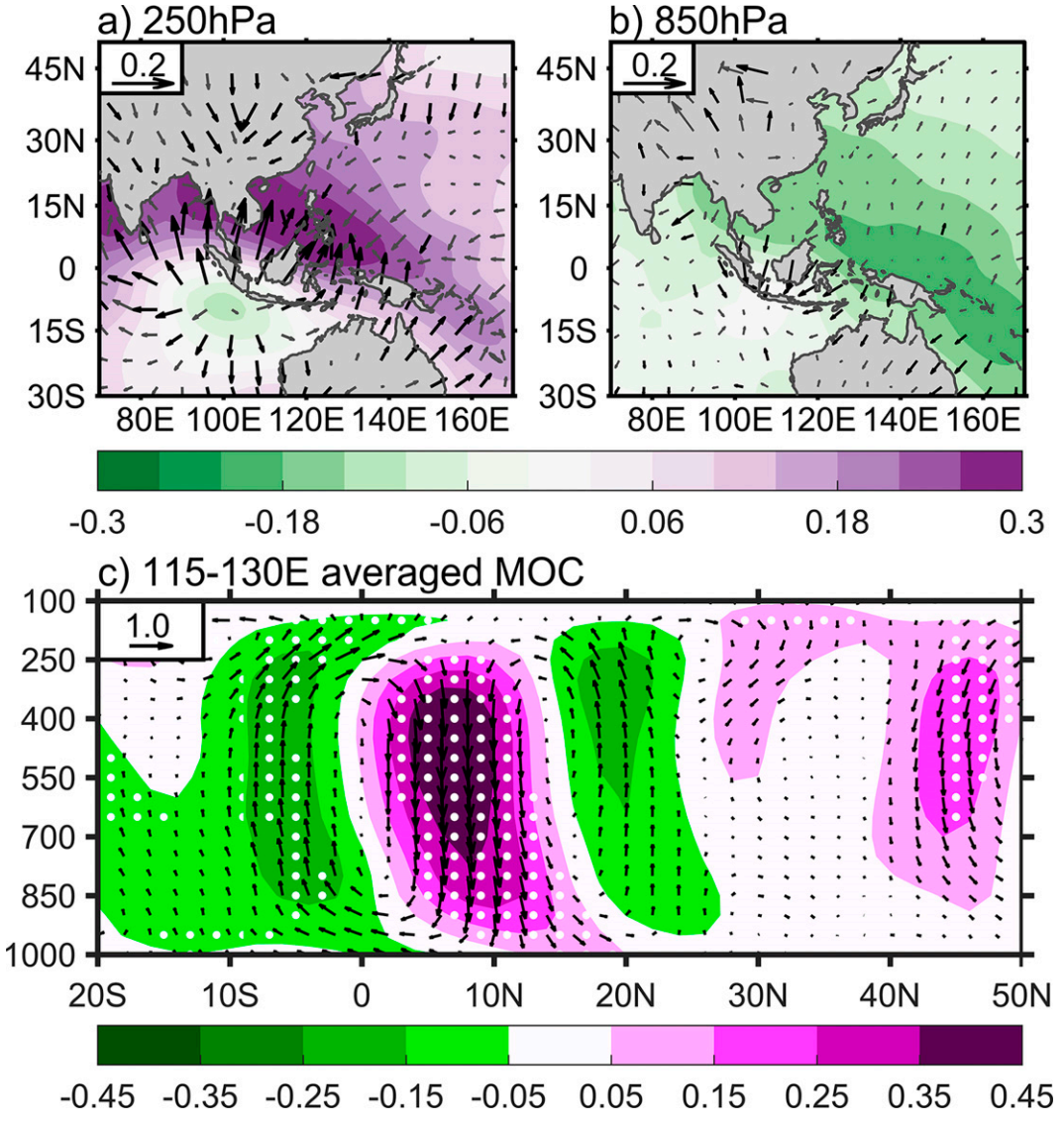

FIG. 7. (a) Regression of the 250-hPa velocity potential (shading; 10^6 m^2 s^{-1}) and divergent wind (vectors; m s^{-1}) anomalies onto the standardized MC SST index. (b) As in (a), but for the 850-hPa level. Thick vectors in (a) and (b) are significant at the 90% confidence level. (c) Atmospheric meridional atmospheric circulation computed from the meridional divergent wind (horizontal component of vectors; m s^{-1}) and vertical velocity (vertical component of vectors and shading; Pa s^{-1}) regressed upon the normalized MC SST index. The vertical velocity is magnified to 100 times when plotting vectors. White dots denote anomalies significant at the 90% confidence level.

located at the 850-hPa level instead. Surface drag may account for this discrepancy in the strongest levels between divergence and vorticity. Accompanying the largest descending motion (negative heating) at around the 400 hPa, an anomalous baroclinic anticyclone is fixed to the northwest of the cooling under the Matsuno–Gill model (Gill 1980). This anchoring effect of convection embeds the SCS anticyclone in the complicated EASM cell, where the vertically sheared climatological wind is low-level southwesterly and upper-level northeasterly (Fig. 6). The mean meridional rotational winds ($\overline{v}_\psi$) in both levels advect the anomalous vorticity gradient $\left[-\overline{v}_\psi(\partial\zeta'/\partial y)\right]$ to balance the already existing baroclinic signals (Kosaka and Nakamura 2006) and finally lead to a combined structure of barotropic and baroclinic modes (Fig. S5a).

The abnormal SST–convection relation (i.e., weak positive SST anomalies corresponding to negative rainfall anomalies; Figs. 2a and 3a,e) suggests that the SCS suppressed convection is not maintained locally but remotely. Together with large convective variations, the MC SST anomalies establish an atmospheric meridional overturning circulation (MOC), which is depicted by regressing the zonally averaged (115°–130°E) vertical velocity and meridional divergent wind

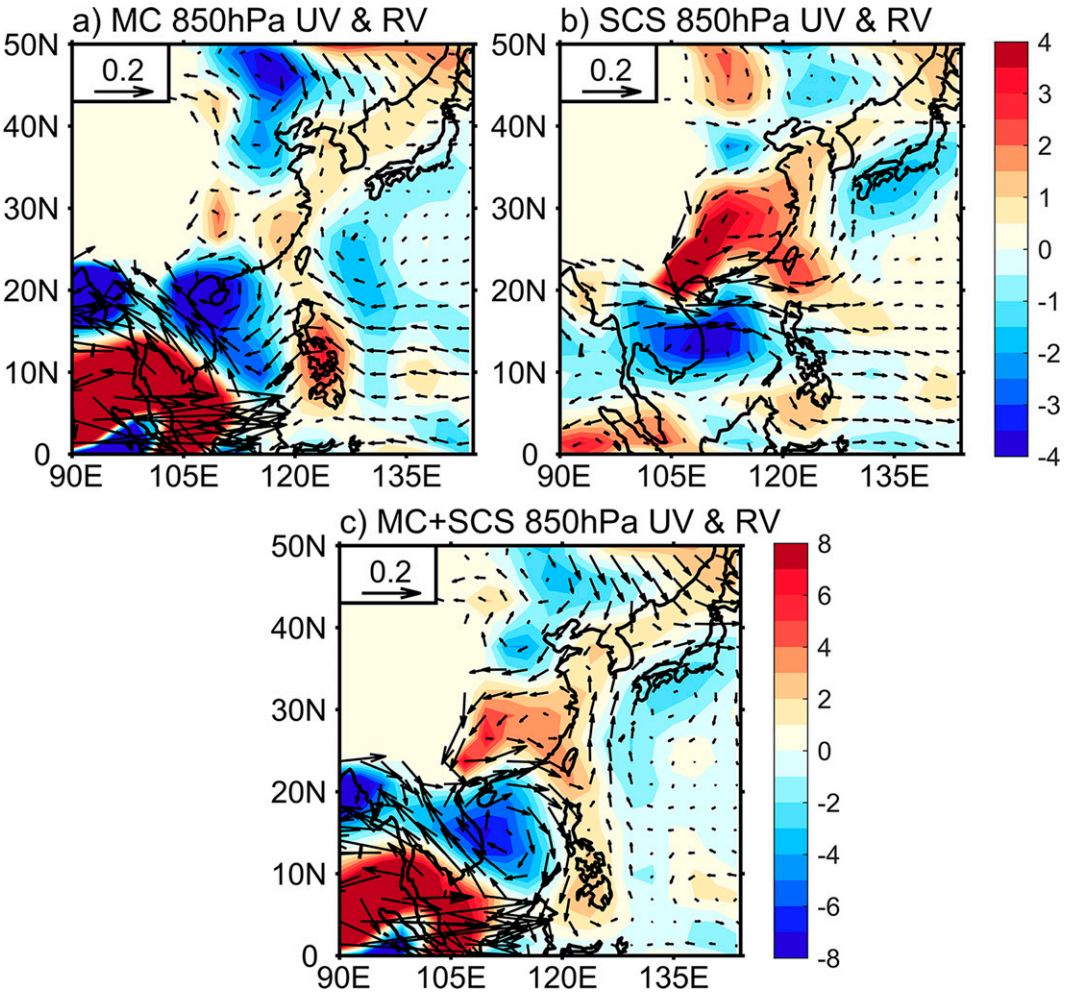

FIG. 8. (a) Responses of 850-hPa winds (vectors; m s^{-1}) and relative vorticity (shading; 10^{-7} s^{-1}) in the MC experiment. (b) As in (a), but for the SCS experiment. (c) Combining (a) and (b).

at each pressure level onto the MC SST index (Fig. 7c). The upward motion over the MC region causes upper-tropospheric divergent flows toward the SCS nearby. The subsidence reaches the maximum ($\partial\omega/\partial p = 0$) in the midtroposphere and is pronounced at 5°–10°N, close to the equator, which further leads to the relatively southward position of the decadal PJ pattern. This MOC is dynamically consistent with the Sverdrup balance: $\beta v \approx f(\partial\omega/\partial p)$, where f is the Coriolis parameter (planetary vorticity) and β is its meridional gradient (Rodwell and Hoskins 2001; Wang et al. 2010); that is, the subsidence over the SCS requires an additional poleward flow ($v > 0$) in the upper troposphere (where $\partial\omega/\partial p > 0$) and an equatorward return flow ($v < 0$) in the lower troposphere (where $\partial\omega/\partial p < 0$) to achieve the closure and maintenance of the MOC. Due to the convection variation residing in the western MC, its limited width restricts the zonal extent of the regional MOC and resultant SCS negative rainfall, so that the decadal PJ pattern is impeded to extend eastward toward the WNP.

The MC variations cannot directly induce a transhemispheric Rossby wave train because there are no strong cross-equatorial flows as a duct for cross-equatorial propagation over the MC–SCS region (Li et al. 2019). Therefore, our analysis indicates that the interhemispheric MOC is crucial for the formation of the decadal PJ teleconnection. Its subsidence over the SCS generates a band of suppressed rainfall. Ensuing divergence together with the anomalous anticyclone acts as a Rossby wave source to relay the MC's influence on East Asia.

c. *Numerical model experiments*

To further validate whether diabatic heating associated with the MC can force the decadal PJ pattern, a series of LBM experiments is conducted. Heating rates are estimated here by the precipitation difference between the positive and negative phases of MC variations and have an elliptical horizontal structure. The maximum heating of the MC experiment imposed at 400 hPa reaches 1.5 K day^{-1}, which corresponds to a 3 mm day^{-1} precipitation difference. Figure 8a shows the

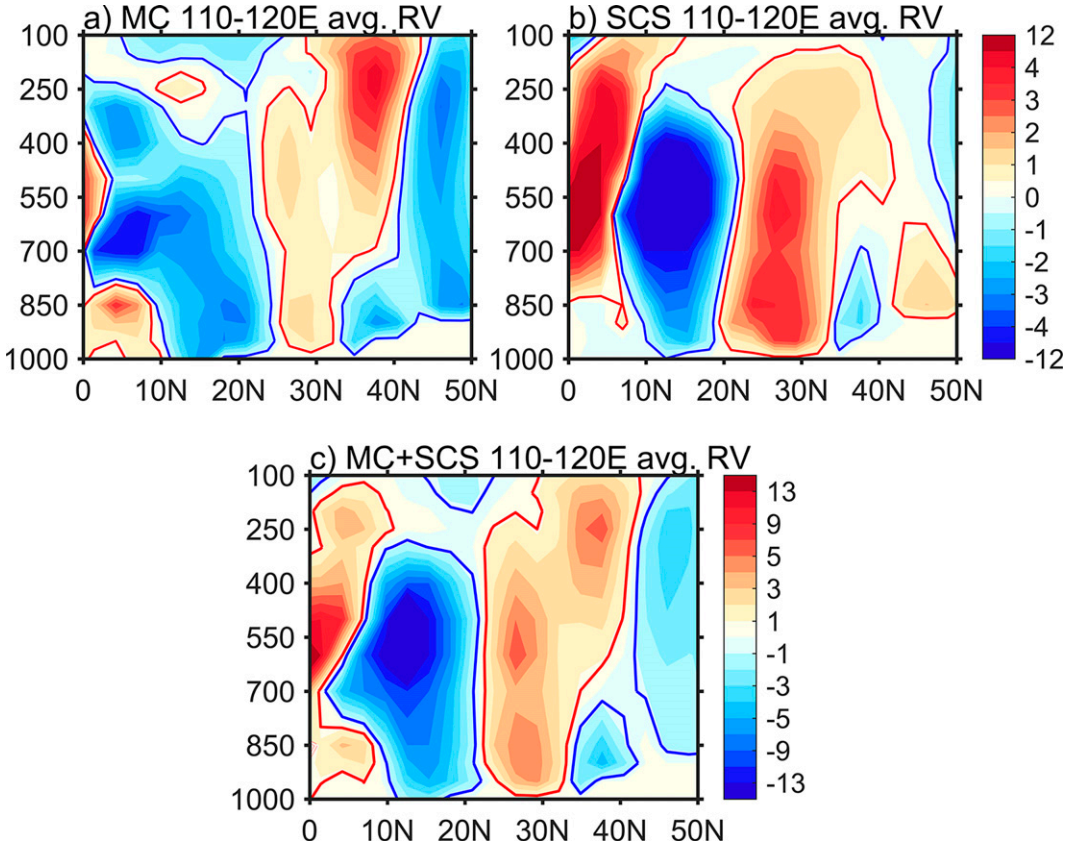

FIG. 9. As in Fig. 8, but for the latitude–height cross section of the relative vorticity (shading; 10^{-7} s^{-1}) averaged over 110°–120°E. For better presentation, in (a) and (b), the contour interval increases from 0.5 × 10^{-7} to 4 × 10^{-7} s^{-1} when the absolute value is above 4 × 10^{-7} s^{-1}. In (c), similarly, the contour interval increases from 1 × 10^{-7} to 2 × 10^{-7} s^{-1} when the absolute value is above 5 × 10^{-7} s^{-1}.

steady response of the 850-hPa relative vorticity and winds from the MC experiment with forcing prescribed over the area 15°S–0°, 90°–120°E. The East Asian circulation exhibits a meridional wavelike pattern, similar to the decadal PJ pattern from observations (Fig. 4a). This teleconnection comprises three major parts, with two anticyclones centered over the SCS and North China and a cyclone over southeastern China. In particular, the zonally averaged (110°–120°E) vorticity profile shows a baroclinic structure south of 10°N and a roughly barotropic structure poleward with a notable northward tilt with height (Fig. 9a). Compared with observations, the amplitude of the cyclone middle of the tripolar pattern is weaker. For the MC experiment, the MC heating can induce upper-level convergence (low-level divergence) over the SCS and generate an anticyclonic circulation there according to vorticity dynamics (Fig. 10a), but it cannot result in suppressed precipitation over the SCS as in reality (Fig. 3e).

Due to the dry LBM lacking the interactive nature between convection generating and large-scale circulation (Watanabe and Jin 2003), the SCS anomalous anticyclone excited by the MC is incapable of inducing an additional negative diabatic heating, which should in turn reinforce the atmospheric anomalies. To offset this deficiency of the dry LBM, we perform a SCS experiment with diabatic cooling prescribed over the area 0°–15°N, 110°–130°E (Fig. 10b). The maximum cooling imposed at the 400 hPa is −0.8 K day^{-1}, which is equivalent to a 1.5 mm day^{-1} precipitation reduction (Fig. S6). In the tropics, an anticyclonic circulation is positioned over the northern SCS as a Gill-type response, and a cyclone with intensified amplitude appears over southeastern China via the poleward dispersion of Rossby wave energy (Fig. 8b). In Fig. 8c, we show that the model result is closer to observations after combining the MC heating and SCS cooling—a meridional wave pattern extending from the SCS to northeastern China can be clearly identified. In the upper layer, outflows from the MC converge on the SCS (Fig. 10c). The latitude–height structure of vorticity (Fig. 9c) resembles observations well (Fig. 5), successfully reproducing the poleward tilt. The dry LBM forced only by the MC heating lacks convection–circulation coupling over the SCS, whereas it is realistically embodied when the negative heating is incorporated. Therefore, these results are supportive of our hypothesis in that the MC variations serve as an engine for the decadal PJ pattern via the SCS anticyclone (suppressed precipitation) functioning as a bridge.

In addition, we conduct more straightforward experiments with CAM4, which involves moist parameterizations and

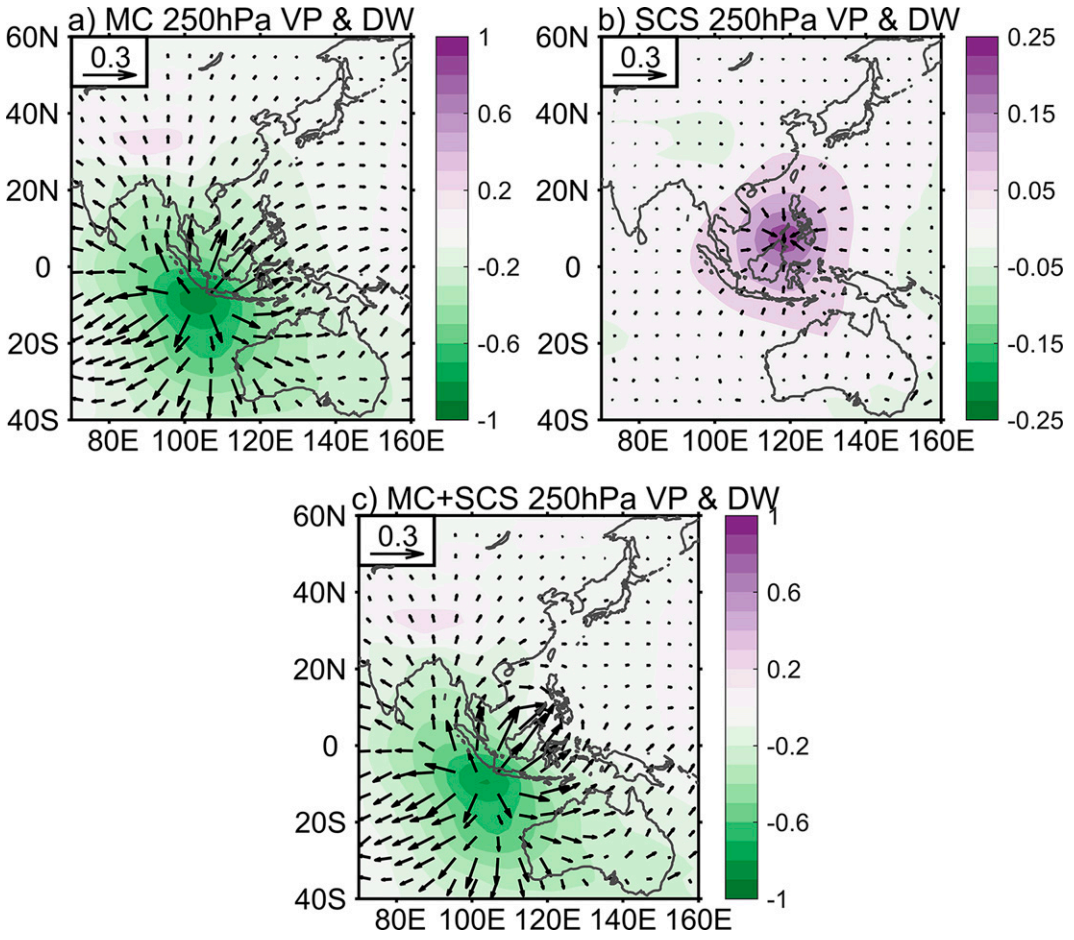

FIG. 10. As in Fig. 8, but for the 250-hPa velocity potential (VP; shading; 10^6 m^2 s^{-1}) and divergent winds (DW; vectors; m s^{-1}).

approaches to the real physics of the atmosphere. The responses of precipitation and 850-hPa winds to MC SST warming are shown in Fig. 11a. Apparently, the MC run well reproduces the decadal PJ pattern with meridionally arranged, tripolar centers along eastern China. In response to the MC SST warming, the cumulus convection in situ is active. Correspondingly, the SCS and North China receive less precipitation, whereas southeastern China joint with Japan receives more precipitation. The cold south–warm north pattern in SAT is also evident over China (Fig. S7). Furthermore, as depicted by the upper-level velocity potential and divergent winds, an enhanced divergence occurs in the MC and flows converge toward the SCS (Fig. 11b). Since there are no strong climatological cross-equatorial flows acting as a waveguide, direct meridional propagation of Rossby waves from the MC in the Southern Hemisphere to the SCS in the Northern Hemisphere is strongly prohibited. Thus, the transhemispheric MOC functions like the Hadley cell, produces subsidence remotely, and physically connects the decadal PJ pattern to the MC SST (Fig. 11c). Note that the model underestimates the amplitude of precipitation over the SCS, which is comparable to the MC counterpart in the reanalysis. A possible explanation is that the precipitation anomaly over the SCS is influenced by multiple factors actually, whereas the experiment here just singles out the part associated with the MC. Overall, the CAM4 results well simulate the decadal PJ pattern and its climate impacts, reflecting the direct forcing of the MC SST. The thermal-forcing experiments from both the CAM4 and the LBM bear close resemblance to observations, suggesting that our proposed mechanism is reasonable.

5. Conclusions and discussion

a. Conclusions

In this study, the role of the MC SST decadal variations in affecting the decadal PJ pattern, the leading mode of summer East Asian vorticity anomaly, is detected in the 20CR dataset and is further confirmed by observational datasets and model experiments. Encircled by the warmest climatological SST, the MC region is a primary latent heat engine driving the tropical atmosphere. On decadal time scales, the rainfall–SST relation over the MC is significant with the correlation

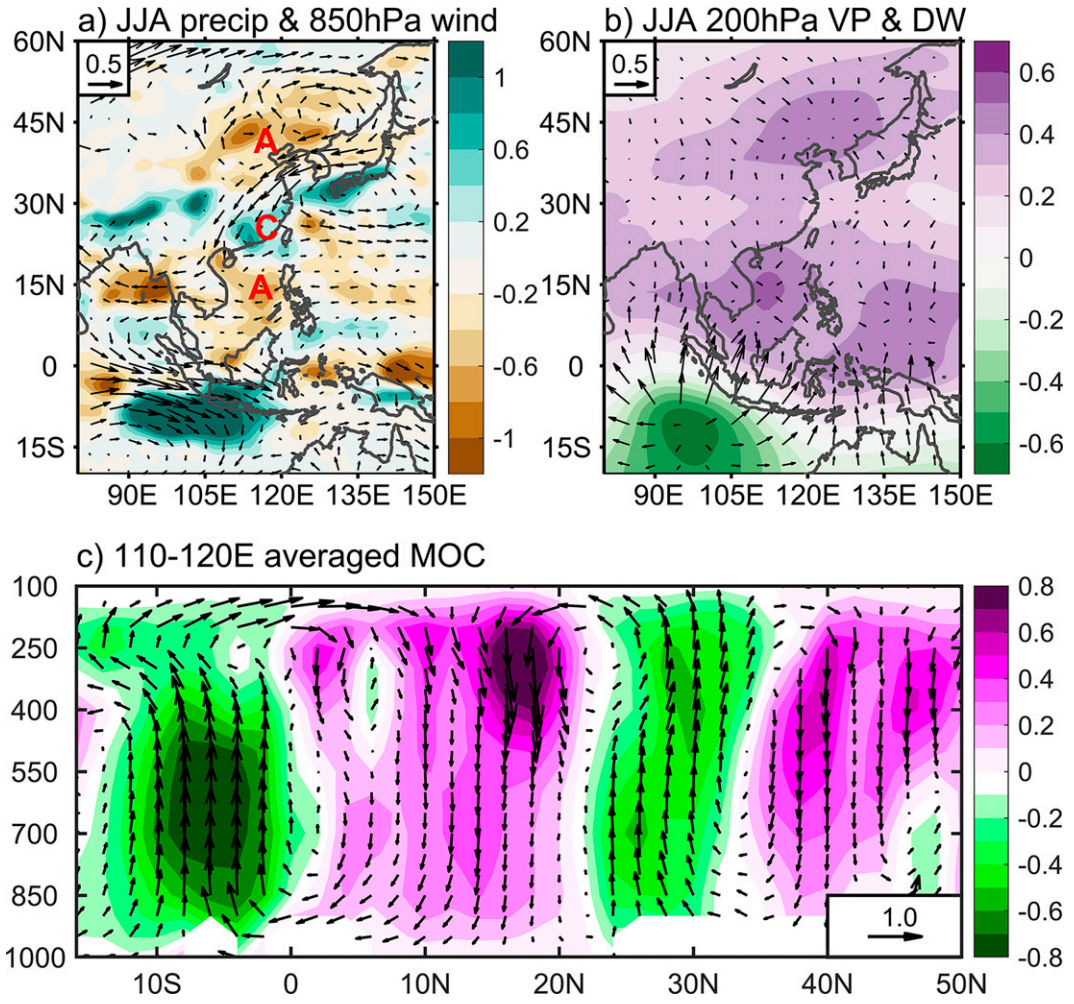

FIG. 11. The JJA mean differences between the CAM4 MC and Control runs. (a) Precipitation (shading; mm day^{-1}) and 850-hPa wind anomalies (vectors; m s^{-1}), (b) 200-hPa velocity potential (shading; 10^6 m^2 s^{-1}) and divergent winds (vectors; m s^{-1}), and (c) atmospheric meridional circulation computed from the meridional divergent wind (horizontal component of vectors; m s^{-1}) and vertical velocity (vertical component of vectors and shading; Pa s^{-1}). The vertical velocity is magnified to 100 times when plotting vectors.

coefficient reaching 0.7, implying that the underlying SST variations can act as a pacemaker of convective variations. Driven by the MC SST-induced convection, the divergent wind in the upper troposphere flows northward into the SCS, where it converges and feeds the subsidence there (Fig. 12). Moreover, the Sverdrup vorticity balance initiates a low-level southward flow toward the equator and hence maintains the tropical atmospheric MOC. In response to the suppressed convection resulting from the subsidence, an anomalous anticyclone, which is the tropical lobe of the decadal PJ pattern, emerges over the SCS. The lower tropospheric divergence further works as a Rossby wave source, forming the ensuing meridional tripolar wave pattern along the coasts of China. The other two parts of the decadal PJ pattern are an anomalous cyclone centered over Taiwan and an anomalous anticyclone over the Bohai Sea.

The decadal PJ pattern has some similarities with the typical PJ pattern. For instance, they both stem from tropical convection, and share the vertical structure with poleward tilting. The low-layer vorticity inclines northward as it propagates into the upper troposphere by about a quarter wavelength. This slanted structure identifies the two PJ pattern as a combination of the baroclinic and barotropic modes. Nevertheless, in contrast with the typical PJ pattern, the decadal PJ pattern shows a more equatorward location, a zonally confined range within the SCS and eastern China, and straight northward propagation of wave energy. These differences are tightly related to several properties of the excitation source (i.e., the MC) and surroundings. Since the tropical MOC is mainly maintained by the western MC convection south of the equator, the resultant major rainfall anomalies are positioned more equatorward and meridionally aligned in the west of

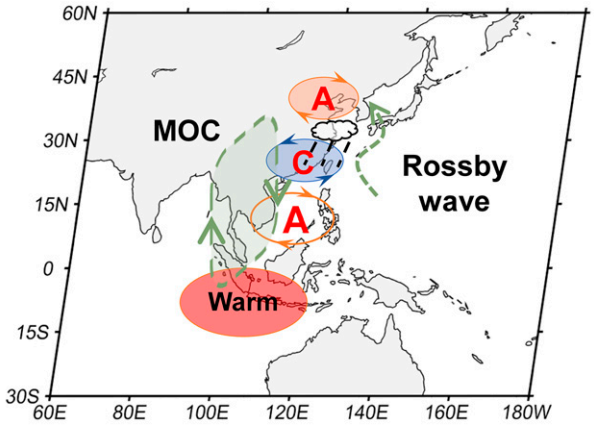

FIG. 12. A schematic diagram for the relationship between the MC SST and the decadal PJ pattern. The MC warm SST anomaly (the red patch over the MC) induces local convection, which generates a meridional circulation with descending motion over the SCS. The descending motion forms the SCS anticyclone. Together with divergence in the lower layer, this low-latitude anticyclone acts as a Rossby wave source, emanating the decadal PJ wave train from the SCS to northeastern China. The orange and blue patches denote the warm and cold SAT there, respectively.

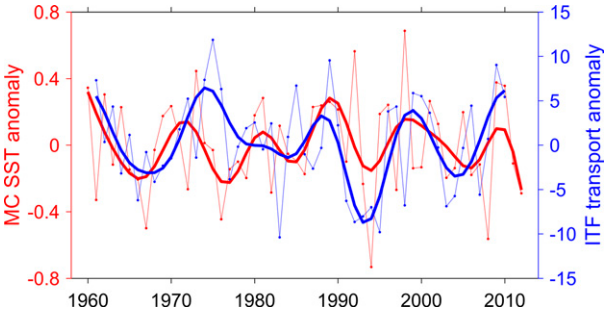

FIG. 13. ITF transport anomaly (blue lines; Sv; 1 Sv $\equiv 10^6$ m^3 s^{-1}) and MC SST anomaly (red lines; °C) on interannual time scales (thin lines) and decadal time scales (thick lines) in which the variability lower than 7 years has been removed.

130°E. This meridional rainfall configuration separates the decadal PJ pattern from the domain of westerly jets (EAWJ and NPLWJ), which further hinders the eastward deflection of wave rays.

The formation mechanism of the decadal PJ pattern is reproduced by both CAM4 and the dry LBM experiments. When only imposing heating over the MC, the LBM simulates a meridional wave train with a poleward-tilted vertical structure. The horizontal pattern is also similar to observations, except for the underestimated amplitude of the anomalous cyclone over southeastern China. In reality, there is a secondary suppressed convection, which is absent in the dry LBM, in response to the anticyclone and subsidence over the SCS. After mimicking this process by prescribing a negative heating in the SCS, both of the modeled structure and amplitude of vorticity resemble the observational counterparts well (Fig. 5). Thus, the LBM model clearly shows the interhemispheric impacts of the MC convective heating on the East Asian circulation and the role of the resultant SCS anticyclone in relaying and amplifying those impacts. The foregoing pathway is further validated by the CAM4 experiments in which only MC SST anomalies are imposed. The results clearly indicate that the MC anomaly alone is enough to induce the whole decadal PJ pattern via convection–circulation coupling.

The MC SST variations and East Asian climate are interrelated via the decadal PJ pattern. Corresponding to the upward motion and advection induced by the cyclone, dynamically consistent cold SAT and above-normal precipitation anomalies emerge over southeastern China. Analogously, the anticyclone over North China produces warm SAT and below-normal precipitation anomalies (Fig. 12). Thus, the MC SST/convection variations bring decadal climate predictability to East Asia, and further evaluation on this predictability is needed, such as with the help of CMIP experiments.

b. *Discussion*

Our analysis elucidates that the decadal PJ pattern can be efficiently forced by the SCS suppressed convection, which results from the MC's convection at root. The tropical SST forcing is indeed an indispensable factor in sustaining the atmospheric teleconnection on decadal to multidecadal time scales (e.g., Zhang et al. 2018). However, above results mentioned that the upper-layer vorticity of the decadal PJ pattern exhibits a well-marked zonal vorticity dipole stretching across the Tibetan Plateau to central China (Fig. 4b). The dipole, which intersects with the decadal PJ pattern, seems beyond the tropical forcing and enhances the cyclonic anomaly over central China. To explore this preliminarily, we applied an EOF analysis to the low-pass-filtered summer vorticity at 200 hPa in the region bounded by 30°–40°N, 80°–120°E. The second EOF mode corresponds to the dipolar structure. Then, the 200-hPa vorticity anomalies regressed onto the second standardized principal component show that the dipole is a part of an extratropical wave train propagating from Europe southeastward to East Asia (Fig. S8). Although this wave train ought to be independent to the MC variations, its signal is detected in the regression with respect to the MC SST index, which may be partly due to their random co-occurrence and the sample size problem. Nevertheless, the climate impacts of this wave train need to be further investigated.

This study mainly focuses on the decadal variability of the MC SST. Thus, one question inevitably comes to mind: what causes its decadal variability? The Indonesian Throughflow (ITF) is a gateway that connects tropical ocean basins and it advects high-temperature water of the western Pacific warm pool southwestward to the region we care about. A half-century long time series of the ITF is reconstructed by Hu and Sprintall (2016, 2017) (Fig. 13). Their ITF transport anomaly is the ensemble mean calculated from oceanic temperature and salinity of objective analysis and assimilation datasets (EN4, GFDL-ECDA, and ORAS3) and verified by direct ITF transport estimates. The correlation coefficient

between decadal variations of the ITF transport and the MC SST is 0.42, which is significant at the 95% confidence level. The coefficient will increase to 0.67 if we ignore the discordance near the 1970s climate regime shift. It is also worth noting that their correlation is nearly zero on interannual time scales (thin lines in Fig. 13). Thus, the ITF transport may be potentially a persistent source activating the MC SST variations on decadal time scales in contrast to interannual time scales. Physically, the ITF transport is driven by the pressure gradient between the Pacific and the Indian Ocean, and many oceanic processes are involved. The related attribution is beyond the scope of our paper and deserves future study to clarify how the Indo–Pacific oceanic circulation change reflects the MC SST variations.

Acknowledgments. The authors sincerely appreciate the constructive comments from reviewers and all data/model providers and archives listed in section 2. They also thank Dr. Shijian Hu for generously sharing the ITF time series. M. Xie is deeply indebted to Jia-Zhen Wang of SCSIO for his kind assistance. This study is jointly supported by the National Natural Science Foundation of China (41731173 and 42006033), the National Key R&D Program of China (2019YFA0606701), the Strategic Priority Research Program of the Chinese Academy of Sciences (XDB42000000 and XDA20060502), the Key Special Project for Introduced Talents Team of Southern Marine Science and Engineering Guangdong Laboratory (Guangzhou) (GML2019ZD0306), the Innovation Academy of South China Sea Ecology and Environmental Engineering, the Chinese Academy of Sciences (ISEE2021ZD01), and the Leading Talents of Guangdong Province Program. The numerical simulation is supported by the High Performance Computing Division in the South China Sea Institute of Oceanology.

REFERENCES

Chen, W., L. Wang, J. Feng, Z. Wen, T. Ma, X. Yang, and C. Wang, 2019: Recent progress in studies of the variabilities and mechanisms of the East Asian monsoon in a changing climate. *Adv. Atmos. Sci.*, **36**, 887–901, https://doi.org/10.1007/s00376-019-8230-y.

Chen, X., and T. Zhou, 2014: Relative role of tropical SST forcing in the 1990s periodicity change of the Pacific-Japan pattern interannual variability. *J. Geophys. Res. Atmos.*, **119**, 13 043–13 066, https://doi.org/10.1002/2014JD022064.

Chung, P.-H., C.-H. Sui, and T. Li, 2011: Interannual relationships between the tropical sea surface temperature and summertime subtropical anticyclone over the western North Pacific. *J. Geophys. Res.*, **116**, D13111, https://doi.org/10.1029/2010JD015554.

Compo, G. P., and Coauthors, 2011: The Twentieth Century Reanalysis Project. *Quart. J. Roy. Meteor. Soc.*, **137** (654), 1–28, https://doi.org/10.1002/qj.776.

Ding, Y., Z. Wang, and Y. Sun, 2008: Inter-decadal variation of the summer precipitation in East China and its association with decreasing Asian summer monsoon. Part I: Observed evidences. *Int. J. Climatol.*, **28**, 1139–1161, https://doi.org/10.1002/joc.1615.

Du, Y., L. Yang, and S.-P. Xie, 2011: Tropical Indian Ocean influence on northwest Pacific tropical cyclones in summer following strong El Niño. *J. Climate*, **24**, 315–322, https://doi.org/10.1175/2010JCLI3890.1.

Geng, Q., A. Sumi, and A. Numaguti, 2000: Role of transients in the dynamics of East Asian summer seasonal mean circulation anomalies—A study of 1993 and 1994. *J. Climate*, **13**, 3511–3529, https://doi.org/10.1175/1520-0442(2000)013<3511:ROTITD>2.0.CO;2.

Gent, P. R., and Coauthors, 2011: The Community Climate System Model version 4. *J. Climate*, **24**, 4973–4991, https://doi.org/10.1175/2011JCLI4083.1.

Gill, A. E., 1980: Some simple solutions for heat-induced tropical circulation. *Quart. J. Roy. Meteor. Soc.*, **106**, 447–462, https://doi.org/10.1002/qj.49710644905.

Harris, I., T. J. Osborn, P. Jones, and D. Lister, 2020: Version 4 of the CRU TS monthly high-resolution gridded multivariate climate dataset. *Sci. Data*, **7**, 109, https://doi.org/10.1038/s41597-020-0453-3.

Hu, K., G. Huang, and R. Huang, 2011: The impact of tropical Indian Ocean variability on summer surface air temperature in China. *J. Climate*, **24**, 5365–5377, https://doi.org/10.1175/2011JCLI4152.1.

Hu, S., and J. Sprintall, 2016: Interannual variability of the Indonesian throughflow: The salinity effect. *J. Geophys. Res. Oceans*, **121**, 2596–2615, https://doi.org/10.1002/2015JC011495.

——, and ——, 2017: Observed strengthening of interbasin exchange via the Indonesian seas due to rainfall intensification. *Geophys. Res. Lett.*, **44**, 1448–1456, https://doi.org/10.1002/2016GL072494.

Huang, B., and Coauthors, 2017: Extended Reconstructed Sea Surface Temperature, version 5 (ERSSTv5): Upgrades, validations, and intercomparisons. *J. Climate*, **30**, 8179–8205, https://doi.org/10.1175/JCLI-D-16-0836.1.

Huang, R., 1992: The East Asia/Pacific pattern teleconnection of summer circulation and climate anomaly in East Asia. *Acta Meteor. Sin.*, **6**, 25–37.

——, and W. Li, 1987: Influence of the heat source anomaly over the western tropical Pacific on the subtropical high over East Asia. *Proc. Int. Conf. on the General Circulation of East Asia*, Chengdu, China, Institute of Atmospheric Physics, Chinese Academy of Sciences, 40–51.

——, and F. Sun, 1992: Impacts of the tropical western Pacific on the East Asian summer monsoon. *J. Meteor. Soc. Japan*, **70**, 243–256, https://doi.org/10.2151/jmsj1965.70.1B_243.

——, J. Chen, L. Wang, and Z. Lin, 2012: Characteristics, processes, and causes of the spatio-temporal variabilities of the East Asian monsoon system. *Adv. Atmos. Sci.*, **29**, 910–942, https://doi.org/10.1007/s00376-012-2015-x.

Jin, F., and B. J. Hoskins, 1995: The direct response to tropical heating in a baroclinic atmosphere. *J. Atmos. Sci.*, **52**, 307–319, https://doi.org/10.1175/1520-0469(1995)052<0307:TDRTTH>2.0.CO;2.

Jones, P. D., and A. Moberg, 2003: Hemispheric and large-scale surface air temperature variations: An extensive revision and an update to 2001. *J. Climate*, **16**, 206–223, https://doi.org/10.1175/1520-0442(2003)016<0206:HALSSA>2.0.CO;2.

——, D. H. Lister, T. J. Osborn, C. Harpham, M. Salmon, and C. P. Morice, 2012: Hemispheric and large-scale land-surface air temperature variations: An extensive revision and an update to 2010. *J. Geophys. Res.*, **117**, D05127, https://doi.org/10.1029/2011JD017139.

Kim, J.-S., R. C.-Y. Li, and W. Zhou, 2012: Effects of the Pacific–-Japan teleconnection pattern on tropical cyclone activity and extreme precipitation events over the Korean peninsula. *J.*

Geophys. Res., **117**, D18109, https://doi.org/10.1029/2012JD017677.

Kosaka, Y., and H. Nakamura, 2006: Structure and dynamics of the summertime Pacific–Japan teleconnection pattern. *Quart. J. Roy. Meteor. Soc.*, **132**, 2009–2030, https://doi.org/10.1256/qj.05.204.

——, and ——, 2010: Mechanisms of meridional teleconnection observed between a summer monsoon system and a subtropical anticyclone. Part I: The Pacific–Japan pattern. *J. Climate*, **23**, 5085–5108, https://doi.org/10.1175/2010JCLI3413.1.

——, S.-P. Xie, and H. Nakamura, 2011: Dynamics of interannual variability in summer precipitation over East Asia. *J. Climate*, **24**, 5435–5453, https://doi.org/10.1175/2011JCLI4099.1.

——, ——, N. C. Lau, and G. A. Vecchi, 2013: Origin of seasonal predictability for summer climate over the northwestern Pacific. *Proc. Natl. Acad. Sci. USA*, **110**, 7574–7579, https://doi.org/10.1073/pnas.1215582110.

Kurihara, K., and T. Tsuyuki, 1987: Development of the barotropic high around Japan and its association with Rossby wave-like propagations over the North Pacific: Analysis of August 1984. *J. Meteor. Soc. Japan*, **65**, 237–246, https://doi.org/10.2151/jmsj1965.65.2_237.

Laloyaux, P., and Coauthors, 2018: CERA-20C: A coupled reanalysis of the twentieth century. *J. Adv. Model. Earth Syst.*, **10**, 1172–1195, https://doi.org/10.1029/2018MS001273.

Lau, K.-M., and L. Peno, 1992: Dynamics of atmospheric teleconnections during the northern summer. *J. Climate*, **5**, 140–158, https://doi.org/10.1175/1520-0442(1992)005<0140:DOATDT>2.0.CO;2.

Lee, S.-K., C. Wang, and B. E. Mapes, 2009: A simple atmospheric model of the local and teleconnection responses to tropical heating anomalies. *J. Climate*, **22**, 272–284, https://doi.org/10.1175/2008JCLI2303.1.

Li, Y., J. Feng, J. Li, and A. Hu, 2019: Equatorial windows and barriers for stationary Rossby wave propagation. *J. Climate*, **32**, 6117–6135, https://doi.org/10.1175/JCLI-D-18-0722.1.

Lu, R., and Z. Lin, 2009: Role of subtropical precipitation anomalies in maintaining the summertime meridional teleconnection over the western North Pacific and East Asia. *J. Climate*, **22**, 2058–2072, https://doi.org/10.1175/2008JCLI2444.1.

——, and S. Lu, 2014: Local and remote factors affecting the SST–precipitation relationship over the western North Pacific during summer. *J. Climate*, **27**, 5132–5147, https://doi.org/10.1175/JCLI-D-13-00510.1.

Lyu, K., J.-Y. Yu, and H. Paek, 2017: The influences of the Atlantic multidecadal oscillation on the mean strength of the North Pacific subtropical high during boreal winter. *J. Climate*, **30**, 411–426, https://doi.org/10.1175/JCLI-D-16-0525.1.

Menne, M. J., C. N. Williams, B. E. Gleason, J. J. Rennie, and J. H. Lawrimore, 2018: The Global Historical Climatology Network monthly temperature dataset, version 4. *J. Climate*, **31**, 9835–9854, https://doi.org/10.1175/JCLI-D-18-0094.1.

Nitta, T., 1987: Convective activities in the tropical western Pacific and their impact on the Northern Hemisphere summer circulation. *J. Meteor. Soc. Japan*, **65**, 373–390, https://doi.org/10.2151/jmsj1965.65.3_373.

Oh, J.-H., B.-M. Kim, K.-Y. Kim, H.-J. Song, and G.-H. Lim, 2013: The impact of the diurnal cycle on the MJO over the Maritime Continent: A modeling study assimilating TRMM rain rate into global analysis. *Climate Dyn.*, **40**, 893–911, https://doi.org/10.1007/s00382-012-1419-8.

Pyper, B. J., and R. M. Peterman, 1998: Comparison of methods to account for autocorrelation in correlation analyses of fish data. *Can. J. Fish. Aquat. Sci.*, **55**, 2127–2140, https://doi.org/10.1139/f98-104.

Rayner, N. A., and Coauthors, 2003: Global analyses of sea surface temperature, sea ice, and night marine air temperature since the late nineteenth century. *J. Geophys. Res.*, **108**, 4407, https://doi.org/10.1029/2002JD002670.

Rodwell, M. J., and B. J. Hoskins, 2001: Subtropical anticyclones and summer monsoons. *J. Climate*, **14**, 3192–3211, https://doi.org/10.1175/1520-0442(2001)014<3192:SAASM>2.0.CO;2.

Sardeshmukh, P. D., and B. I. Hoskins, 1984: Spatial smoothing on the sphere. *Mon. Wea. Rev.*, **112**, 2524–2529, https://doi.org/10.1175/1520-0493(1984)112<2524:SSOTS>2.0.CO;2.

Schneider, U., P. Finger, A. Meyer-Christoffer, E. Rustemeier, M. Ziese, and A. Becker, 2017: Evaluating the hydrological cycle over land using the newly-corrected precipitation climatology from the Global Precipitation Climatology Centre (GPCC). *Atmosphere*, **8**, 52, https://doi.org/10.3390/atmos8030052.

Song, F., and T. Zhou, 2015: The crucial role of internal variability in modulating the decadal variation of the East Asian summer monsoon–ENSO relationship during the twentieth century. *J. Climate*, **28**, 7093–7107, https://doi.org/10.1175/JCLI-D-14-00783.1.

Sui, C.-H., P.-H. Chung, and T. Li, 2007: Interannual and interdecadal variability of the summertime western North Pacific subtropical high. *Geophys. Res. Lett.*, **34**, L11701, https://doi.org/10.1029/2006GL029204.

Sun, W., and Coauthors, 2021: The assessment of global surface temperature change from 1850s: The C-LSAT2.0 ensemble and the CMST-Interim datasets. *Adv. Atmos. Sci.*, **38**, 875–888, https://doi.org/10.1007/s00376-021-1012-3.

Takaya, K., and H. Nakamura, 2001: A formulation of a phase-independent wave-activity flux for stationary and migratory quasigeostrophic eddies on a zonally varying basic flow. *J. Atmos. Sci.*, **58**, 608–627, https://doi.org/10.1175/1520-0469(2001)058<0608:AFOAPI>2.0.CO;2.

Ting, M., and L. Yu, 1998: Steady response to tropical heating in wavy linear and nonlinear baroclinic models. *J. Atmos. Sci.*, **55**, 3565–3582, https://doi.org/10.1175/1520-0469(1998)055<3565:SRTTHI>2.0.CO;2.

Tsuyuki, T., and K. Kurihara, 1989: Impact of convective activity in the western tropical Pacific on the East Asian summer circulation. *J. Meteor. Soc. Japan*, **67**, 231–247, https://doi.org/10.2151/jmsj1965.67.2_231.

Wang, B., 2000: Pacific–East Asian teleconnection: How does ENSO affect East Asian climate? *J. Climate*, **13**, 1517–1536, https://doi.org/10.1175/1520-0442(2000)013<1517:PEATHD>2.0.CO;2.

——, Q. Ding, X. Fu, I.-S. Kang, K. Jin, J. Shukla, and F. Doblas-Reyes, 2005: Fundamental challenge in simulation and prediction of summer monsoon rainfall. *Geophys. Res. Lett.*, **32**, L15711, https://doi.org/10.1029/2005GL022734.

Wang, C., 2019: Three-ocean interactions and climate variability: A review and perspective. *Climate Dyn.*, **53**, 5119–5136, https://doi.org/10.1007/s00382-019-04930-x.

——, S.-K. Lee, and C. R. Mechoso, 2010: Interhemispheric influence of the Atlantic warm pool on the southeastern Pacific. *J. Climate*, **23**, 404–418, https://doi.org/10.1175/2009JCLI3127.1.

Watanabe, M., and M. Kimoto, 2000: Atmosphere–ocean thermal coupling in the North Atlantic: A positive feedback. *Quart. J.*

Roy. Meteor. Soc., **126**, 3343–3369, https://doi.org/10.1002/qj.49712657017.

——, and F.-F. Jin, 2002: Role of Indian Ocean warming in the development of Philippine Sea anticyclone during ENSO. *Geophys. Res. Lett.*, **29**, 1478, https://doi.org/10.1029/2001GL014318.

——, and ——, 2003: A moist linear baroclinic model: Coupled dynamical–convective response to El Niño. *J. Climate*, **16**, 1121–1139, https://doi.org/10.1175/1520-0442(2003)16<1121:AMLBMC>2.0.CO;2.

Willmott, C. J., and K. Matsuura, 2001: Terrestrial air temperature and precipitation: Monthly and annual time series (1950–1999) (version 1.02), http://climate.geog.udel.edu/~climate/.

Wu, B., and T. Zhou, 2008: Oceanic origin of the interannual and interdecadal variability of the summertime western Pacific subtropical high. *Geophys. Res. Lett.*, **35**, L13701, https://doi.org/10.1029/2008GL034584.

——, ——, and T. Li, 2009: Contrast of rainfall–SST relationships in the western North Pacific between the ENSO-developing and ENSO-decaying summers. *J. Climate*, **22**, 4398–4405, https://doi.org/10.1175/2009JCLI2648.1.

——, ——, and ——, 2016: Impacts of the Pacific–Japan and circumglobal teleconnection patterns on the interdecadal variability of the East Asian summer monsoon. *J. Climate*, **29**, 3253–3271, https://doi.org/10.1175/JCLI-D-15-0105.1.

Xie, M., and C. Wang, 2020: Decadal variability of the anticyclone in the western North Pacific. *J. Climate*, **33**, 9031–9043, https://doi.org/10.1175/JCLI-D-20-0008.1.

Xie, S.-P., K. Hu, J. Hafner, H. Tokinaga, Y. Du, G. Huang, and T. Sampe, 2009: Indian Ocean capacitor effect on Indo–western Pacific climate during the summer following El Niño. *J. Climate*, **22**, 730–747, https://doi.org/10.1175/2008JCLI2544.1.

——, Y. Kosaka, Y. Du, K. Hu, J. S. Chowdary, and G. Huang, 2016: Indo-western Pacific Ocean capacitor and coherent climate anomalies in post-ENSO summer: A review. *Adv. Atmos. Sci.*, **33**, 411–432, https://doi.org/10.1007/s00376-015-5192-6.

Xu, P., L. Wang, W. Chen, J. Feng, and Y. Liu, 2019: Structural changes in the Pacific–Japan pattern in the late 1990s. *J. Climate*, **32**, 607–621, https://doi.org/10.1175/JCLI-D-18-0123.1.

Xu, Q., and Z. Guan, 2017: Interannual variability of summertime outgoing longwave radiation over the Maritime Continent in relation to East Asian summer monsoon anomalies. *J. Meteor. Res.*, **31**, 665–677, https://doi.org/10.1007/s13351-017-6178-3.

Yang, S., T. Zhang, Z. Li, and S. Dong, 2019: Climate variability over the Maritime Continent and its role in global climate variation: A review. *J. Meteor. Res.*, **33**, 993–1015, https://doi.org/10.1007/s13351-019-9025-x.

Zhang, H., Z. Wen, R. Wu, Z. Chen, and Y. Guo, 2017: Interdecadal changes in the East Asian summer monsoon and associations with sea surface temperature anomaly in the South Indian Ocean. *Climate Dyn.*, **48**, 1125–1139, https://doi.org/10.1007/s00382-016-3131-6.

Zhang, Y., S.-P. Xie, Y. Kosaka, and J.-C. Yang, 2018: Pacific decadal oscillation: Tropical Pacific forcing versus internal variability. *J. Climate*, **31**, 8265–8279, https://doi.org/10.1175/JCLI-D-18-0164.1.